Journal of Power Sources 244 (2013) 214–221

Contents lists available at SciVerse ScienceDirect

Journal of Power Sources

journal homepage: www.elsevier.com/locate/jpowsour

A Li-ion battery using $LiMn_2O_4$ cathode and MnO_x/C anode

Changju Chae [a], Hongyeol Park [a], Dongwook Kim [a], Jongsik Kim [b], Eun-Suok Oh [c], Jung Kyoo Lee [a,*]

[a] Department of Chemical Engineering, Dong-A University, Busan 604-714, Republic of Korea
[b] Department of Chemistry, Dong-A University, Busan 604-714, Republic of Korea
[c] School of Chemical Engineering and Bioengineering, University of Ulsan, Ulsan 680-749, Republic of Korea

HIGHLIGHTS

- A MnO_x/C nanocomposite was prepared by a facile process as a high capacity anode.
- MnO_x/C anode was combined with $LiMn_2O_4$ (LMO) cathode into a full cell LIB.
- The new LMO-MnO_x/C battery operates at 3.3 V on average with a capacity of 105 mAh g^{-1}.
- The LMO-MnO_x/C battery delivered the reversible capacity of LMO for up to 245 cycles.
- The LMO-MnO_x/C battery also exhibited an appreciable rate capability up to 2 C rate.

GRAPHICAL ABSTRACT

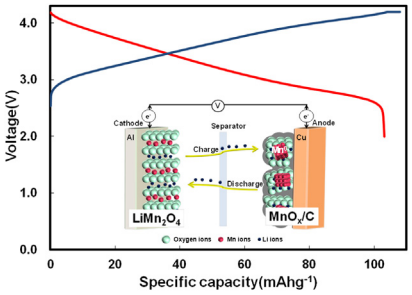

ARTICLE INFO

Article history:
Received 3 October 2012
Received in revised form
25 January 2013
Accepted 29 January 2013
Available online 9 February 2013

Keywords:
Manganese oxides
Li-ion battery anode
Mesoporous carbon
Lithium manganese oxide
Manganese oxides carbon composite

ABSTRACT

MnO_x/C nanocomposite, in which MnO_x nanocrystals (64 wt%, mainly MnO with Mn_3O_4 phase) 5–30 nm in size are formed *in situ* in the confined pores of a preformed mesoporous carbon, is prepared by a facile process. The morphology and structure of MnO_x/C are characterized using N_2 adsorption/desorption measurement, scanning electron microscopy (SEM), transmission electron microscopy (TEM), X-ray diffraction (XRD), X-ray photoelectron spectroscopy (XPS), and thermogravimetric analysis (TGA). As an anode for Li-ion batteries (LIB), the MnO_x/C delivers the theoretical capacity of MnO_x (700–750 mAh g^{-1} at 100 mA g^{-1}) with excellent rate capability. MnO_x/C prelithiated is combined with a delithiated $LiMn_2O_4$ (LMO) cathode for a complete Li-ion battery cell in a charged state with a cathode limiting capacity. The LMO-MnO_x/C cell exhibits reversible capacity of the LMO cathode, with the cycling stability and rate capability dependent upon those of the MnO_x/C anode. An LMO-MnO_x/C cell with anode loading in slight excess delivers reversible capacity of LMO without capacity fading for up to 245 cycles, and exhibits an appreciable rate capability at 2 C. The LMO-MnO_x/C configuration can be developed as a reliable LIB, potentially offering low cost, high rate capability, safety, and reliability.

1. Introduction

Energy storage systems based on lithium ion batteries (LIB) are being explored to go beyond current popular uses of powering small consumer electric devices, to emerging large-scale applications, such as electric vehicles, energy storage for renewable sources, and many other industrial applications [1–3]. These

* Corresponding author. Tel.: +82 51 200 7718; fax: +82 51 200 7728.
E-mail addresses: jklee88@dau.ac.kr, jklducheme@gmail.com (J.K. Lee).

0378-7753/$ – see front matter © 2013 Elsevier B.V. All rights reserved.
http://dx.doi.org/10.1016/j.jpowsour.2013.01.157

emerging applications necessitate more advanced characteristics than those offered by current LIBs, including high energy and power density, low cost, improved safety and reliability [1–5]. Various cathode materials that offer much improved characteristics in terms of energy and power density, safety, and cost over conventional $LiCoO_2$ have been suggested [6–13]. Among them, $LiMn_2O_4$ (LMO), which forms a spinel structure, can offer high rate capability owing to the 3D lattice for lithium intercalation and deintercalation paths. It also has highly appealing properties, such as low cost, non-toxicity, environmental compatibility, and safety [6,7,14]. More advanced Mn-spinels include Al-doped [15,16] and Ni-substituted spinels [14,17–20], which are respectively characterized by stable cycling at elevated temperature and high voltage operation.

On the anode side, graphitic carbon has long been predominantly used as the anodes for commercial lithium ion batteries, because of its excellent cycling stability and low cost. However, graphitic carbon anode material has low theoretical capacity (372 mAh g^{-1} with one Li per C_6), and poor rate capability, due to a low intrinsic Li intercalation rate into its lattice crystal structure ($d = 3.35$ Å), which raises safety concerns at high rate charging due to lithium plating, and relatively low volumetric capacity. Hence, it has become a crucial issue to develop advanced anode material that provides higher capacity (both volumetric and specific), and faster charging capability than graphitic carbon. Transition metal oxides (TMO) could be potential candidates due to their high conversion capacity, high intrinsic density, abundance, and non-toxicity [21–27]. In particular, manganese oxides (MnO_x) possess a much lower reduction voltage plateau (around 0.5 V vs. Li^+/Li) due to lower electromotive force, and thus, higher energy density when coupled with specific cathodes than other TMO [27–32]. MnO_x also offers much higher theoretical conversion capacity (756–1233 mAh g^{-1}) than graphitic carbon anodes [28–30,32]. However, MnO_x has poor electrochemical reversibility due to extremely low electrical conductivity and drastic chemical and structural changes that inherently accompany the conversion reactions during charge and discharge processes [24,33,34]. Among various routes to mitigate these inherent problems, MnO_x incorporation into nanostructured composites with a conducting matrix such as carbon could be one of the most promising approaches.

In this study, we prepared MnO_x/C nanocomposite, in which MnO_x nanocrystals of size in the 5–30 nm range were formed *in situ* in the pores of a mesoporous carbon by a simple bottom-up approach, which involves the impregnation of MnO_x precursor solution onto a preformed mesoporous carbon, followed by a mild thermal annealing in Ar [25,32]. MnO_x/C exhibited a theoretical capacity of MnO_x (*i.e.*, reversible capacity of MnO with minor contribution from Mn_3O_4 phase in the composite: 700–750 mAh g^{-1} at 100 mA g^{-1}), with excellent cycling performance and rate capability. For practical evaluation of the anode materials, it would be highly desirable to test the electrochemical responses in a full cell configuration with a specific cathode [35–39]. For this purpose, LMO-MnO_x/C full cells were assembled to evaluate MnO_x/C as an anode with a cathode limiting capacity [38,39]. The LMO-MnO_x/C full cell exhibited stable cycling performance with excellent rate performance. This electrode configuration could be a highly attractive candidate for applications requiring high power, low cost, and reliability.

2. Experimental

2.1. Materials and reagents

Resorcinol (≥99.0%), formaldehyde (~37 wt% in H_2O), and $Mn(NO_3)_2 \cdot 5H_2O$ (≥98%) were purchased from Sigma–Aldrich, and Na_2CO_3 (≥99.5%) and HF (48 wt% in H_2O) were purchased from Junsei Chemical. Silica nanoparticles (15 nm in diameter, Sigma–Aldrich) were used as a template for mesoporous carbon. All chemicals were used as received.

2.2. Preparation of mesoporous carbon and MnO_x/C

Mesoporous carbon (MC) was prepared by carbonizing a resorcinol-formaldehyde (RF) carbon gel polymer containing silica nanoparticles as a template, which was described previously [25]. In short, silica template (3.2 g) was dispersed in DI water (42 ml) in a glass vial. Resorcinol (1.4 g), formaldehyde (2.0 ml of 37 wt% in water), and sodium carbonate solution (1.2 ml of 0.2 M solution in water) were added into the silica solution. The mixture was stirred until all the chemicals were dissolved, and heated at 90 °C in a sealed vial to form a gel. The composite gel was further aged at 90 °C overnight and thoroughly washed with DI water and filtered. The dried composite gel was heated to 850 °C (at 5 °C min^{-1}) in a tube furnace in Ar flow, and maintained at 850 °C for 2 h. The composite was treated with HF (15 wt%) to dissolve the silica template. The residual carbon was thoroughly washed with DI water, filtered, and dried to obtain the MC.

A manganese precursor, $Mn(NO_3)_2 \cdot 5H_2O$, was dissolved in DI water (4.8 M). An amount of Mn precursor solution, equivalent to the pore volume of MC, was impregnated onto MC, and the Mn-impregnated/MC was dried at 80 °C in air. This process was repeated until the desired MnO_x loading on MC was obtained. The dried sample was heated in Ar flow to 450 °C (at 5 °C min^{-1}) and maintained at 450 °C for 2 h to yield MnO_x/C.

2.3. Characterizations

The powder X-ray diffraction (XRD) patterns of samples were recorded on an Ultima IV, Rigaku model D/MAX-50kV system (Cu-K_α radiation, $\lambda = 1.5418$ Å). The morphologies of samples were investigated using field-emission scanning electron microscopy (FE-SEM, JEOL JSM-35CF operated at 10 kV) and transmission electron microscopy (TEM, JEOL JEM-2010 operated at 200 kV). N_2 adsorption/desorption isotherm measurement was performed on a Micromeritics AS1-A4 system at liquid nitrogen temperature. Brunauer-Emmett-Teller (BET) and Barrett-Joyner-Halenda (BJH) methods were used to estimate the BET surface area and pore size distribution, respectively. X-ray photoelectron spectroscopy (XPS) was performed on a Thermo Electron Corporation spectrometer with an Al K_α (1486.6 eV) radiation. The carbon content in MnO_x/C was determined by weight loss in thermogravimetric analysis (TGA) run to 800 °C at a ramping rate of 10 °C min^{-1} in an air flow.

2.4. Electrochemical measurements

Electrochemical tests were performed using CR2032 coin cells with Li foil as the counter electrode. The working electrode of MnO_x/C was prepared by casting a paste that consisted of 80 wt% active material (MnO_x/C), 10 wt% conductive additive (Super P Li, Timcal Ltd.), and 10 wt% poly(vinylidene fluoride) (PVDF) binder dissolved in anhydrous N-methyl-2-pyrollidone onto a copper foil using a Meyer-Bar Coating Device (Kipae E&T, Korea). The coated electrodes were roll-pressed and then vacuum dried at 80 °C for 12 h. A commercial $LiMn_2O_4$ (LMO, Phoenix materials Co., Ltd., Korea) electrode was prepared by casting a slurry composed of 85.0 wt% active material, 7.5 wt% conductive additive (Super P Li, Timcal Ltd.) and 7.5 wt% PVDF binder dissolved in anhydrous N-methyl-2-pyrollidone onto Al foil. The coated electrodes were roll-pressed and then vacuum dried at 120 °C for 12 h. A Celgard 2400 polypropylene membrane was used as the separator. 1 M $LiPF_6$ in an

ethylene carbonate/dimethyl carbonate (EC/DMC) mixture (3:7 v/v) provided by Panax Etec Co., Ltd. (Korea) was used as the electrolyte. The cells were assembled in an argon-filled glove box. The MnO_x/C cells were galvanostatically cycled on a galvanostat (WonATech Co., Ltd., Korea) over a voltage range of 3.0–0.02 V vs. Li^+/Li. Cyclic voltamograms were recorded on a potentiostat (WonATech, Korea) over a voltage range of 3.0–0.02 V vs. Li^+/Li at a scan rate of 0.1 mV s^{-1}. The LMO cells were galvanostatically cycled over a voltage range of 4.5–3.3 V vs. Li^+/Li at a current of 0.2 C (1 C = 148 mA g^{-1}) rate.

Prior to full Li-ion cell assembling, the MnO_x/C for the anode and LMO for the cathode were lithiated and delithiated over the aforementioned voltage ranges using a Swagelok-type cell with Li foil as the counter electrode. These working electrodes were reassembled into a Swagelok-type full cell in a charged state in the glove box using the same separator and electrolyte as in the half cell assembly. Two full cells were assembled with different active material loadings of 4.5 and 1.2 mg cm^{-2} (LMO-MnO_x/C (A)) or 3.7 and 1.8 mg cm^{-2} (LMO-MnO_x/C (B)) for the LMO cathode and the MnO_x/C anode, respectively. The cells were galvanostatically cycled in a voltage range of 4.1–2.0 V at a current density of 0.2 C rate relative to the cathode mass.

3. Results and discussion

3.1. Materials characterizations

The morphology of MC was examined by SEM, and the images are shown in Fig. 1. The high magnification SEM image of MC in Fig. 1b indicates that 10–20 nm pores were developed due to the isolated silica nanoparticles (15 nm) used as the template, together with large pores generated from silica template aggregates. Fig. 1c and d show the nitrogen adsorption/desorption isotherms and pore size distribution of MC, respectively. The hysteresis in the isotherms over the pressure range (P/P_0 = 0.4–0.9) indicated the presence of mesopores. The calculated BJH pore size distribution based on the desorption isotherm of MC showed mesopores below 12 nm in diameter with a preponderance of ~4 nm mesopores. The BET surface area was 1060 m^2 g^{-1}, and the total pore volume at P/P_0 = 0.97 was 1.06 cm^3 g^{-1}. The high surface area also suggested that a significant amount of micropores was present in MC, which is most often generated by carbonization of the resorcinol resin [40]. Thus, this simple process using RF gel composite embedded with commercial silica template yielded a mesoporous carbon which has highly desirable physical properties (a high surface area with mesopores and a large pore volume) as a support for MnO_x nanocrystals.

The powder X-ray diffraction (XRD) pattern of MnO_x/C in Fig. 2a revealed that manganese precursor was successfully converted into manganese oxides in MC by thermal annealing at 450 °C in Ar flow. The peaks could be indexed to MnO (JCPDS No. 07-0230), with a small portion of Mn_3O_4 (JCPDS No. 24-0734) phase [32]. The average particle size of MnO_x nanocrystals in MnO_x/C samples was estimated from the line width of (200) diffraction using the Scherrer's formula ($D = K\lambda/(\beta \cos\theta)$ with $K = 0.89$ for spheres) to be 23 nm [41]. The surface chemical composition of MnO_x/C was further investigated by X-ray photoelectron spectroscopy, and the result is shown in Fig. 2b. The main peaks observed in the spectra were C1s (284.6 eV), O1s (530.4 eV), and Mn2p. The high-resolution XPS spectrum of the Mn 2p region is shown in the inset of Fig. 2b. The Mn $2p_{1/2}$ and $2p_{3/2}$ signals are located at 654.3 and 614.7 eV, respectively. The values of Mn2p and O1s are in good agreement with the literature values of Mn^{2+} in bulk MnO, supporting that

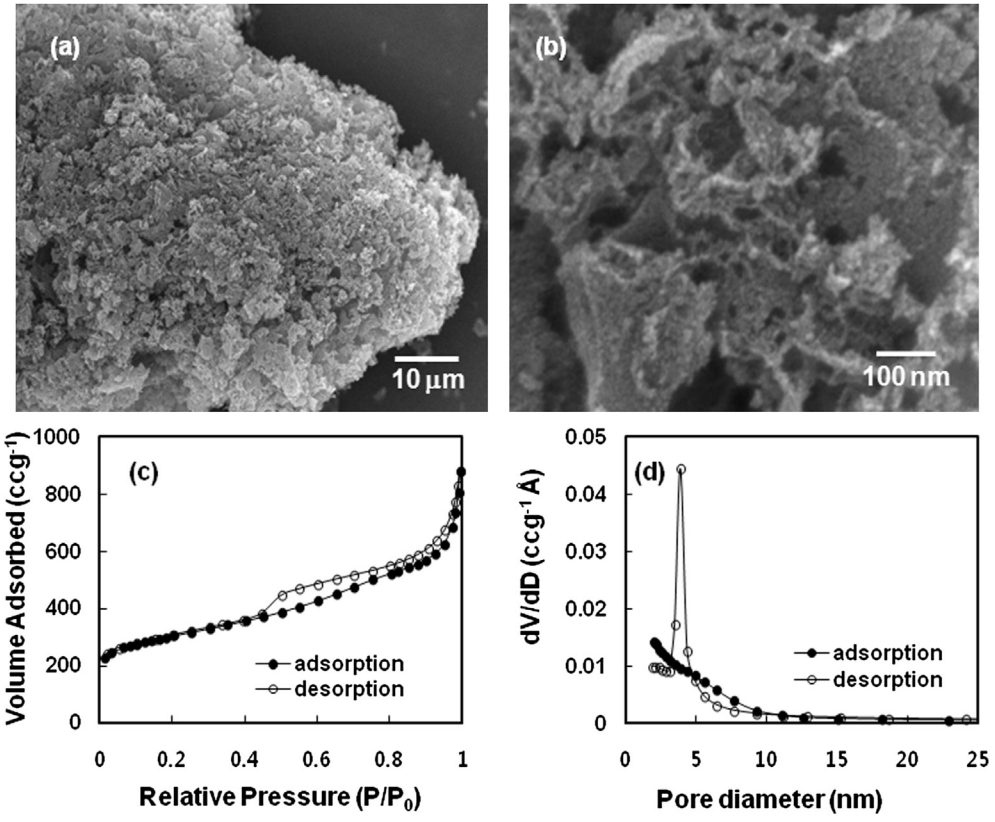

Fig. 1. FE-SEM image of MC at (a) low magnification and (b) high magnification, (c) N_2 adsorption/desorption isotherms, and (d) BJH pore size distribution of MC.

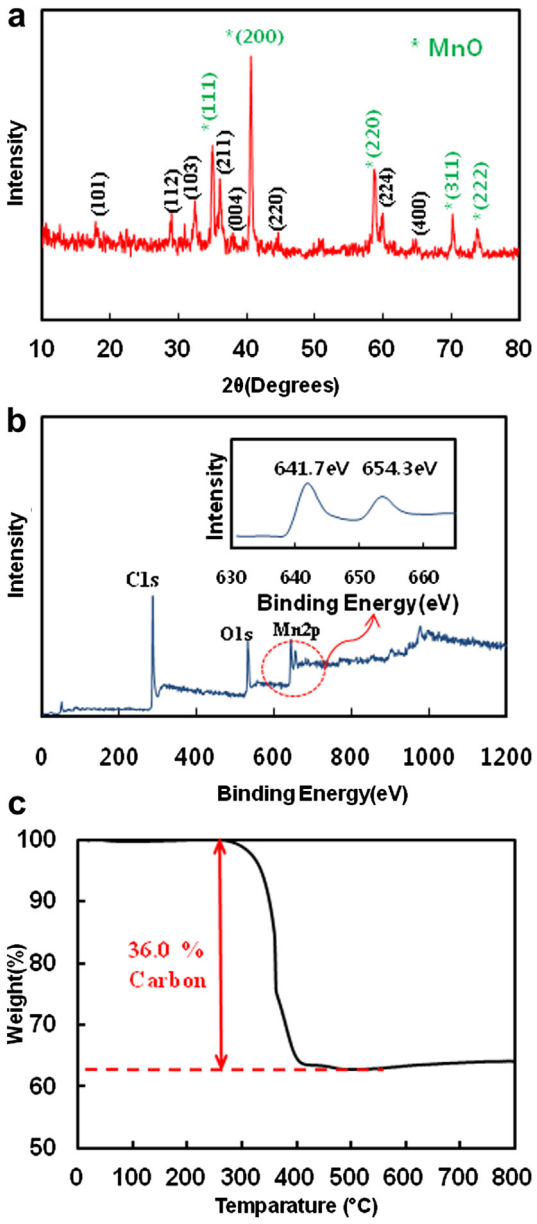

Fig. 2. (a) XRD pattern of MnO_x/C, (b) XPS spectrum of MnO_x/C with a high-resolution spectrum of Mn2p in the inset, (c) TGA profile of MnO_x/C up to 800 °C in an air flow and at a rate of 10 °C min^{-1}.

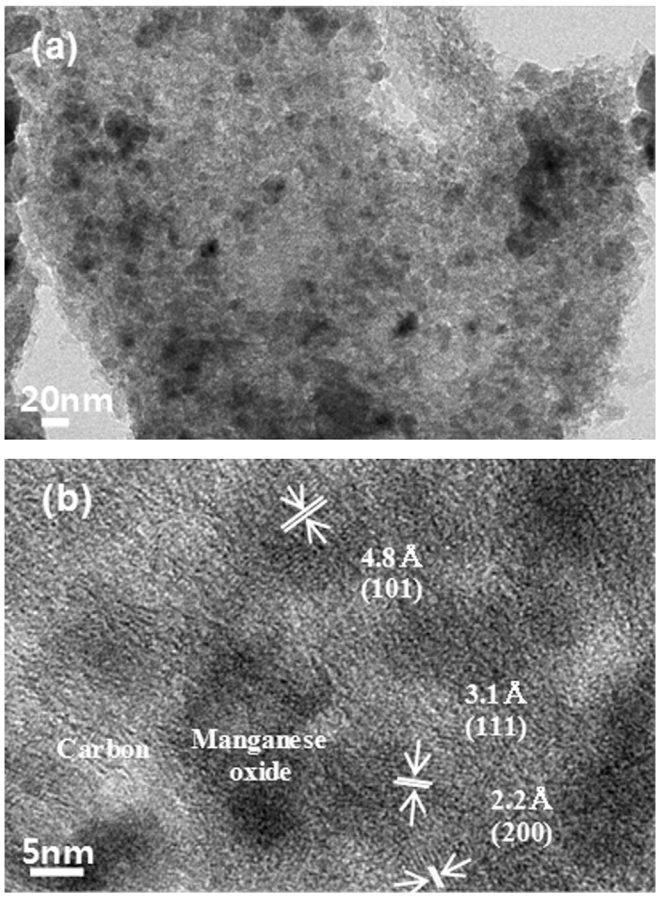

Fig. 3. TEM images of MnO_x/C at (a) low magnification and (b) high magnification.

MnO is the dominant phase on the surface of the MnO_x/C samples [42,43]. The MnO_x content in MnO_x/C was determined by TGA analysis, shown in Fig. 2c, to be about 64 wt%. Fig. 3 shows the TEM images of MnO_x/C. MnO_x nanocrystals with size in the range of 5–30 nm were mostly observed in the confined mesopores of MC (Fig. 3a). The lattice *d*-spacing of 4.8 Å, 3.1 Å, and 2.2 Å corresponding to (101), (111), and (200) planes of MnO, respectively, were identified in the high magnification image in Fig. 3b.

Thus, MnO_x nanocrystals 5–30 nm in size were successfully formed selectively in the confined pores of MC with the MnO_x loading of 64 wt% by the simple *in situ* process employed in this study. Compared to the general multi-step process that includes a separate synthesis of TMO nanocrystals by a solution reduction method, followed by handling of the nanoparticles and a carbon coating step, this process can be easily scaled-up and is highly facile for the preparation of TMO/C nanocomposite with commercially available raw materials. In the as prepared MnO_x/C, MnO_x nanocrystals were also well distributed on MC and physically separated from each other by conductive carbon matrix, which are beneficial in mitigating the aforementioned problems inherent to MnO_x for lithium ion battery applications.

3.2. Electrochemical measurements

3.2.1. Anode material

The electrochemical properties of MnO_x/C were firstly characterized by cyclic voltammetry (CV) tests. In the CV curves of MnO_x/C for the initial three cycles shown in Fig. 4a, three reduction peaks were observed at 0.08, 0.6, and 1.2 V in the first reduction process. The two small peaks at 0.6 and 1.2 V disappeared in the subsequent cycles, suggesting irreversible Li^+ reaction with carbon and metal oxides, and decomposition of the electrolyte forming a solid electrolyte interface (SEI) film [29]. The main spiky peak at 0.08 V could be attributed to the Mn^{2+} and Mn^{3+} (a small portion from Mn^{3+} in Mn_3O_4) reduction to Mn^0 and Li_2O. This distinct peak was shifted to 0.2–0.5 V in the subsequent cycles due to electrode polarization caused by partly irreversible phase transformation between crystalline MnO_x and Li_2O/Mn^0 nanocomposite [44,45]. In the oxidation process, the main peak was recorded at 1.2 V with a weak peak at 2.1 V, corresponding to the oxidation of Mn^0 to Mn^{2+} and Mn^{3+} and decomposition of the formed SEI layer at high oxidation potential above 2.0 V, respectively [44]. Both the reduction and oxidation curves after the first cycle almost overlapped, indicating excellent electrochemical reversibility of the MnO_x nanocrystals in MC. From

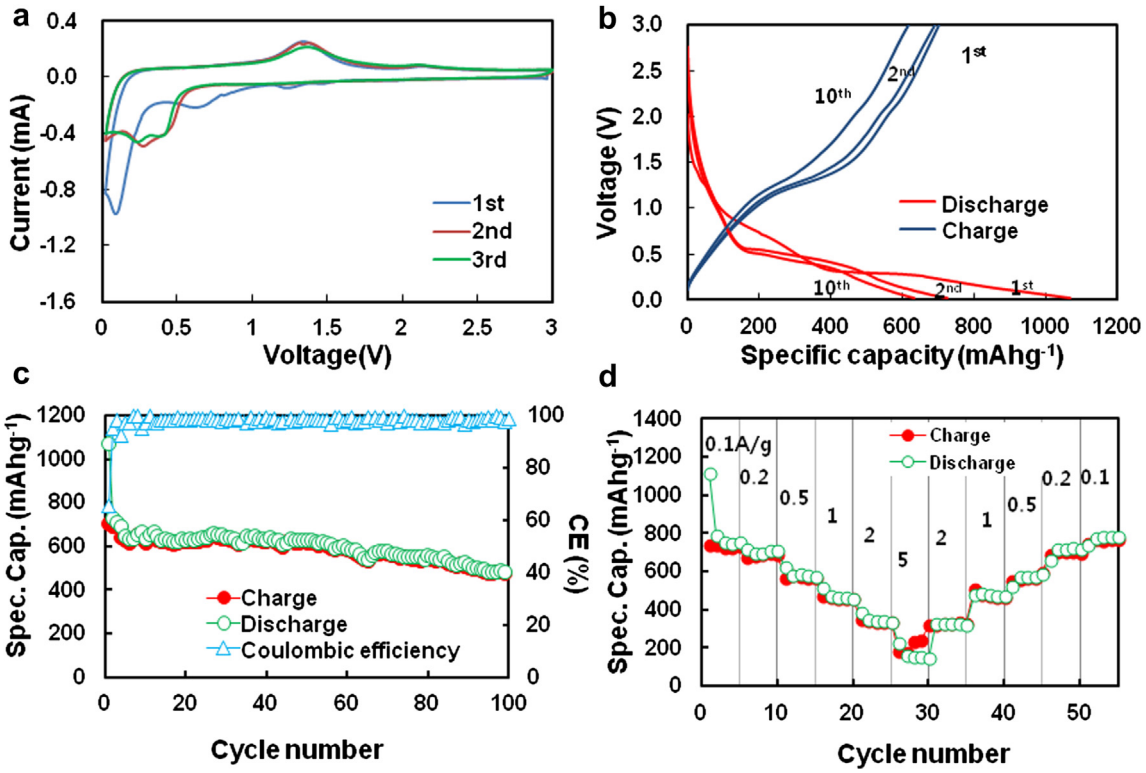

Fig. 4. (a) Cyclic voltammograms of MnO_x/C at a scan rate of 0.1 mV s^{-1}, (b) voltage profiles of MnO_x/C, (c) cycling performance of MnO_x/C between 0.02 and 3.0 V at 100 mA g^{-1} for initial three cycles and then at 200 mA g^{-1} for up to 100 cycles, (d) rate performance of MnO_x/C cycled between 0.02 V and 3.0 V.

the CV test, voltage hysteresis between oxidation (1.2 V) and reduction (0.3 V on average) processes after the first cycle was measured to be around 0.9 V for MnO_x/C. High voltage hysteresis is a common phenomenon for conversion reactions and is a major drawback of TMO, since it induces charge/discharge inefficiency and corresponding energy losses in lithium ion batteries. Nonetheless, MnO_x-based materials possess relatively lower voltage hysteresis than other TMO [25,46].

Fig. 4b presents the voltage profiles of MnO_x/C. In the first discharge, the voltage dropped rapidly to 1.5 V, followed by two small inflection points at 1.5–1.0 V and 1.0–0.4 V, which were absent in the subsequent cycles. A distinct voltage plateau was observed at 0.3 V, followed by a sloping voltage profile between 0.3 and 0.02 V due to the reduction of Mn^{2+}/Mn^{3+} in MnO_x/C to Mn^0, interfacial lithium storage in the grain boundary regions between Li_2O and Mn^0 grains [44,45,47], and lithium storage in the carbon matrix in MnO_x/C. The voltage plateau at 0.3 V was shifted to 0.5 V in the subsequent discharge curves due to electrode polarization caused by irreversible phase transformation between crystalline MnO and Li_2O/Mn^0 [44,45]. The first charge curve showed a sloping plateau at ~1.2 V due to the reverse conversion reaction, and the charge curves in the subsequent cycles overlapped, indicating the reversibility of the electrochemical conversion reaction (1), shown below (for simplicity, MnO_x is assumed to be MnO, since x is close to one according to the analysis results). The first discharge and charge capacities were 1055 and 700 mAh g^{-1}, respectively, accounting for the irreversible capacity loss of 355 mAh g^{-1} and the Coulombic efficiency (CE) of about 66%.

$$MnO + 2Li \leftrightarrow Mn^0 + Li_2O \quad (1)$$

Fig. 4c shows the galvanostatic cycling performance of MnO_x/C, cycled at the current density of 100 mA g^{-1} for the initial three cycles, and then at 200 mA g^{-1} for up to 100 cycles. MnO_x/C exhibited the reversible capacities of 700–750 mAh g^{-1} at 100 mA g^{-1} and 630–660 mAh g^{-1} at 200 mA g^{-1}. Hence, the theoretical capacity of MnO_x (MnO plus Mn_3O_4) can be extracted from MnO_x/C nanocomposite. The capacity was well retained for up to 60 cycles, but a slow capacity fading was observed starting from the 60th cycle, and the capacity retention was decreased down to around 75% after 100 cycles. Fig. 4d presents the rate responses of MnO_x/C cycled at different current densities in the range of 100–5000 mA g^{-1}. The discharge capacities were retained at 700–750, 570–590, and 460–480 mAh g^{-1} at the current densities of 100–200, 500, and 1000 mA g^{-1}, respectively. MnO_x/C still delivered 320–345 mAh g^{-1} even at 2000 mA g^{-1}, while commercial graphite lost most of its theoretical capacity at 1000–2000 mA g^{-1} [32]. However, at the current density of 5000 mA g^{-1}, MnO_x/C showed abnormal behavior of reversed capacity level between discharge and charge, possibly due to the rather poor kinetics associated with the electrochemical conversion reaction (1). When the current was returned to 100 mA g^{-1} after 50 cycles, MnO_x/C exhibited its initial capacity, indicating excellent cycling reversibility of the MnO_x/C nanocomposite.

3.2.2. Cathode material

A commercial LMO was used as the cathode material for a complete Li-ion battery based on manganese oxides on both electrodes. The voltage profile of LMO cycled between 3.3 and 4.5 V vs. Li^+/Li at 0.2 C rate (1 C = 148 mA g^{-1}) is given in Fig. 5a. In the charge and discharge curves, a voltage plateau was observed at around 4.1 V on average according to the electrochemical process (2), shown below. The charge and discharge capacities were 110 and 107 mAh g^{-1}, respectively, corresponding to the CE of 97%.

$$LiMn_2O_4 \leftrightarrow xLi + Li_{1-x}Mn_2O_4 \quad (2)$$

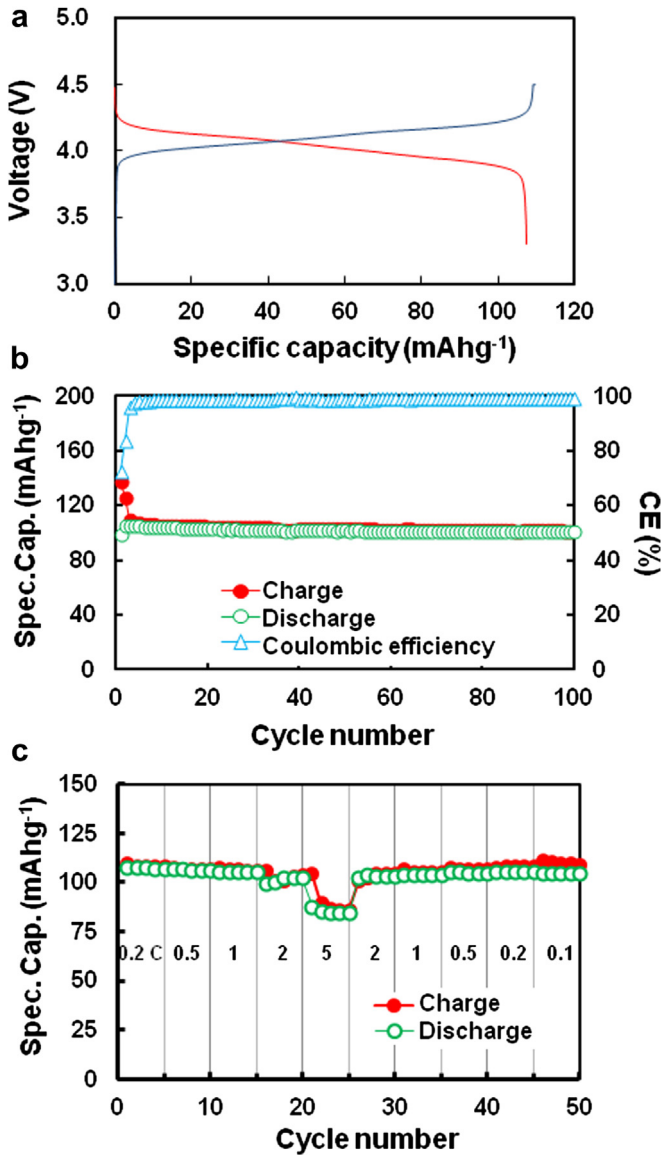

Fig. 5. (a) Voltage profiles of LMO, (b) cycling performance of LMO at a current density of 0.2 C, (c) rate performance of LMO cycled at various current densities. Voltage cut-off range is between 3.3 and 4.5 V vs. Li^+/Li.

Fig. 5b shows the cycling performance of LMO cycled at 0.2 C for 100 cycles. LMO delivered a reversible capacity of 105 mAh g^{-1} with CEs over 97% after the initial conditioning cycles. Its capacity retention after 100 cycles was 96%. The rate performance of LMO cycled at a different rate is shown in Fig. 5c. As expected, LMO exhibited no noticeable capacity loss, even at 1 C rate, and it still delivered 97% of the capacity at 0.1 C even at 2 C. At 5 C, its capacity retention was as high as 79%. Owing to the 3D lattice structure of LMO, high rate capability was exhibited, which is a highly appealing feature of LMO for potential applications requiring high power [6].

3.2.3. Complete Li-ion cell

To demonstrate a manganese oxide-based Li-ion battery, an LMO cathode and an MnO_x/C anode were combined into a complete Li-ion cell. However, the MnO_x/C anode exhibited rather high irreversible capacity loss (Fig. 4b and c), *i.e.*, about 34%, in the first cycle associated with undesirable reactions such as excessive electrolyte decomposition and gaseous products evolution. The first irreversible capacity loss of anode side can cause capacity loss and fading in a full cell combined with a specific cathode. Hence, for the purpose of demonstration and evaluation of electrochemical behavior of a new Li–Mn battery system, LMO-MnO_x/C full cells were assembled in a charged state following the preconditioning procedure described in the experimental section [38,48]. The MnO_x/C electrode can also be partially prelithiated to suppress the irreversible capacity loss by placing it in direct contact with a Li foil wetted with electrolyte [35,39].

Fig. 6a shows the voltage profile of LMO-MnO_x/C (A) cycled between 2.0 and 4.1 V at 0.2 C rate, reflecting the overall electrochemical process (3), shown below. The voltage profiles of LMO-MnO_x/C (A) exhibited steep slopes compared to those of LMO due to the inherent voltage characteristics of MnO_x/C (Fig. 4b). The voltage hysteresis between charge and discharge was lowered to 0.5 V in LMO-MnO_x/C (A) from 0.9 V in the MnO_x/C half cell against Li metal. The reduced polarization, similarly observed in $LiFePO_4$–Fe_2O_3 system [38], may be associated with the decreased energy barrier to the reduction of Mn–O bonds and/or to the re-oxidation of Li_2O/Mn pairs, but further work is needed to clarify this behavior. Nonetheless, it is of worth to remark that the reduced polarization in a complete Li-ion cell with MnO_x/C anode would make it more viable for application. The LMO-MnO_x/C battery operates with an average voltage of 3.3 V and a specific capacity of 105 mAh g^{-1} based on the cathode mass, giving a specific energy density on the order of 350 Wh kg^{-1}.

$$(x/2)\mathrm{MnO/C} + \mathrm{LiMn_2O_4} \leftrightarrow (x/2)\mathrm{Li_2O} + (x/2)\mathrm{Mn^0/C} + \mathrm{Li_{1-x}Mn_2O_4} \quad (3)$$

The cycling performance of LMO-MnO_x/C (A) is presented in Fig. 6b. The capacity was well maintained at around 100 mAh g^{-1} cycled at 0.2 C, but it started to fade slowly from the 60th cycle to give 73% retention after 100 cycles. When the current was lowered to 0.1 C after 100 cycles at 0.2 C, the initial capacity was recovered completely. However, it continued to fade slowly and exhibited around 60% retention after 188 cycles. Considering the highly stable cycling performance of LMO, the capacity fading should be due to the MnO_x/C anode side, which showed capacity fading starting from 60th cycle as well (Fig. 4c). This issue may be addressed by a proper electrolyte composition and suitable binders for MnO_x-based conversion anode materials [49], which will be subjected to future study. The cycling performance of LMO-MnO_x/C (B), which has a higher loading ratio of the anode to cathode material than cell (A), is presented in Fig. 6c. After the initial conditioning cycles for up to 25 cycles, the LMO-MnO_x/C (B) showed stable cycling for up to 195 cycles without capacity fading. The cell was further subjected to rate testing after the 195th cycle, and the result is given in Fig. 6d. Relative to the capacity at 0.1 C, the capacity retentions at 1 C and 2 C rates were 82% and 68%, respectively, while the cell capacity faded with further cycles at 5 C rate, showing a retention as low as 35%. These retention values are inferior to those of the Li-LMO half cell (Fig. 5c), indicating that the rate performance of the LMO-MnO_x/C cell is mostly governed by the anode side. After the rate was returned to 0.1 C, the capacity was completely restored, indicating excellent electrochemical reversibility of the LMO-MnO_x/C system. Overall, the LMO-MnO_x/C full cell exhibited energy density (350 Wh kg^{-1}) comparable to those of commercial LIBs [39]. However, its high rate capability, potentially high volumetric energy density (higher density of MnO_x than graphitic carbon), and the low cost of the materials should be additional benefits provided by the LMO-MnO_x/C configuration.

Hence, we have shown that a nanostructured MnO_x/C can be readily prepared by a facile process using low cost materials. The as prepared MnO_x/C showed highly appealing electrochemical

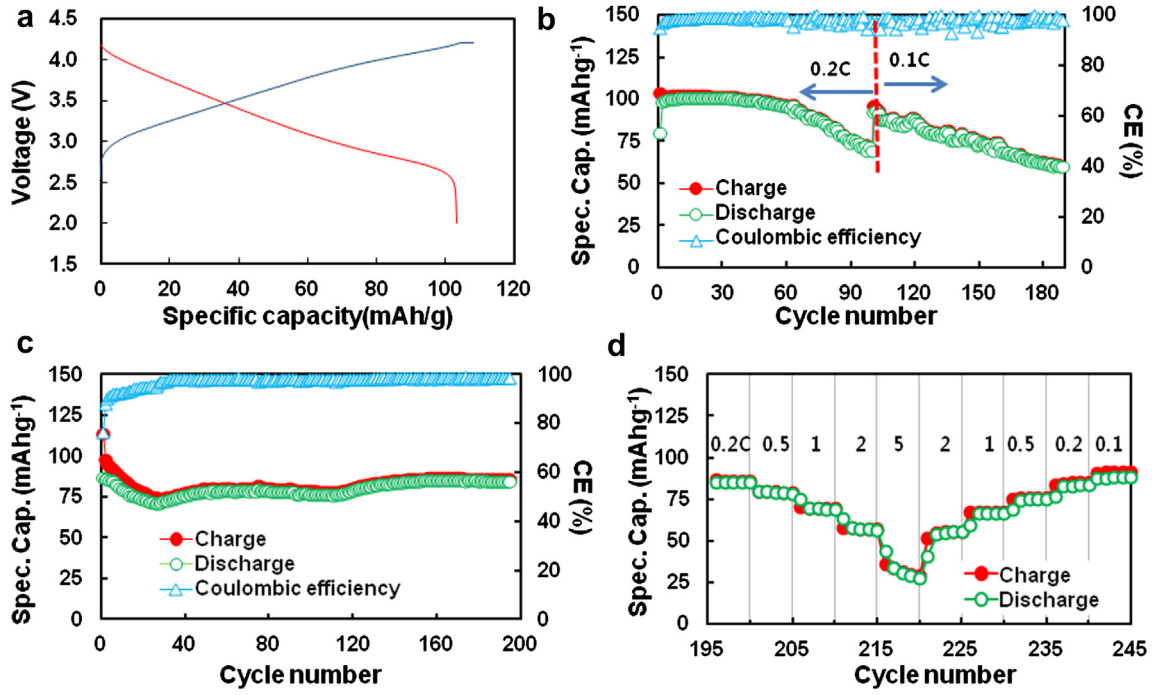

Fig. 6. (a) Voltage profile, (b) cycling performance of LMO-MnO_x/C (A) cell at 0.2 C for 100 cycles and then at 0.1 C for up to 188 cycles, (c) cycling performance of LMO-MnO_x/C (B) cell at 0.2 C for up to 195 cycle, and (d) rate performance of LMO-MnO_x/C (B) cell. Voltage cut-off range is between 2.0 and 4.1 V.

properties as an anode for LIBs. The MnO_x/C anode can be combined with an LMO cathode in a complete Li-ion battery cell featuring low cost, high rate, and reliability. The issues concerning the cycling stability and irreversible capacity loss in the first cycle of MnO_x/C are left to be resolved in the near future.

4. Conclusions

MnO_x/C nanocomposite, in which MnO_x (MnO with Mn_3O_4 phase) nanocrystals with 5–30 nm size were formed *in situ* in the confined pores of a preformed mesoporous carbon, was prepared by a facile process with MnO_x content of 64 wt%. The electrochemical properties of MnO_x/C as an anode for LIBs were investigated in a full cell with an LMO cathode and in a half cell with Li foil as the reference electrode. MnO_x/C delivered the theoretical capacity of MnO_x (around 700–750 mAh g^{-1} at 100 mA g^{-1}) with excellent rate capability. MnO_x/C was combined with a commercial LMO cathode for a complete Li-ion battery cell in a charged state with a cathode limiting capacity. The LMO-MnO_x/C cell exhibited reversible capacity of the LMO cathode, with the cycling stability and rate capability dependent upon those of the MnO_x/C anode. An LMO-MnO_x/C cell (B) with anode loading in slight excess showed highly stable cycling for up to 245 cycles without capacity loss and appreciable rate capability at 2 C. Nonetheless, the issues concerning the cycling stability and irreversible capacity loss in the first cycle of MnO_x/C are left to be resolved in the near future. Overall, the LMO-MnO_x/C configuration can be developed as a reliable LIB, potentially offering low cost, high rate capability, and safety characteristics.

Acknowledgment

This work was supported by a grant from the National Research Foundation of Korea, funded by the Korean Government (MEST) (NRF-2009-C1AAA001-0093307).

References

[1] L. Taberna, S. Mitra, P. Poizot, P. Simon, J.M. Tarascon, Nat. Mater. 5 (2006) 567.
[2] M.S. Whittingham, MRS Bull. 33 (2008) 411.
[3] B. Scrosati, J. Garche, J. Power Sources 195 (2010) 2419.
[4] J. Cabana, L. Monconduit, D. Larcher, M.R. Palacin, Adv. Mater. 22 (2010) E170.
[5] J.M. Tarascon, Philos. Trans. R. Soc. A-Math. Phys. Eng. Sci. 368 (2012) 3227.
[6] B.L. Ellis, K.T. Lee, L.F. Nazar, Chem. Mater. 22 (2010) 691.
[7] J.W. Fergus, J. Power Sources 195 (2010) 939.
[8] M.M. Thackeray, C.S. Johnson, J.T. Vaughey, N. Li, S.A. Hackney, J. Mater. Chem. 15 (2005) 2257.
[9] K.G. Gallagher, S.-H. Kang, S.U. Park, S.Y. Han, J. Power Sources 196 (2011) 9702.
[10] Y.-K. Sun, B.-R. Lee, H.-J. Noh, H. Wu, S.-T. Myung, K. Amine, J. Mater. Chem. 21 (2011) 10108.
[11] S.W. Oh, S.-T. Myung, S.-M. Oh, K.H. Oh, K. Amine, B. Scrosati, Y.-K. Sun, Adv. Mater. 22 (2010) 4842.
[12] J.R. Croy, D. Kim, M. Balasubramanian, K. Gallgher, S.-H. Kang, M.M. Thackeray, J. Electrochem. Soc. 159 (2012) A781.
[13] K. Kang, Y.S. Meng, J. Breger, C.P. Grey, G. Cedar, Science 311 (2006) 977.
[14] F. Jiao, J. Bao, A.H. Hill, P.G. Bruce, Angew. Chem. Int. Ed. 47 (2008) 9711.
[15] Y.S. Lee, M. Yoshio, Electrochem. Solid State Lett. 4 (2001) A155.
[16] Y.G. Xia, Q. Zhang, H.Y. Wang, H. Nakamura, H. Noguchi, M. Yoshio, Electrochim. Acta 52 (2007) 4708.
[17] M. Wakihara, Electrochem. 73 (2005) 328.
[18] M. Kunduraci, G.G. Amatucci, Electrochim. Acta 53 (2008) 4193.
[19] Y. Talyosef, B. Markovsky, G. Salitra, D. Aurbach, H.J. Kim, S. Choi, J. Power Sources 146 (2005) 664.
[20] S.H. Park, S.W. Oh, S.H. Kang, I. Belharouak, K. Amine, Y.K. Sun, Electrochim. Acta 52 (2007) 7226.
[21] P. Poizot, S. Laruelle, S. Grugeon, L. Dupont, J.M. Tarascon, Nature 407 (2000) 496.
[22] H. Zhang, H. Tao, Y. Jiang, Z. Jiao, M. Wu, B. Zhao, J. Power Sources 195 (2010) 2950.
[23] M.-Y. Cheng, B.-J. Hwang, J. Power Sources 195 (2010) 4977.
[24] W.M. Zhang, X.L. Wu, J.S. Hu, Y.G. Guo, L.J. Wan, Adv. Funct. Mater. 18 (2008) 3941.
[25] T. Yoon, C. Chae, Y.K. Sun, X. Zhao, H.H. Kung, J.K. Lee, J. Mater. Chem. 21 (2011) 17325.
[26] H.L. Wang, L.F. Cui, Y.A. Yang, H.S. Casalongue, J.T. Robinson, Y.Y. Liang, Y. Cui, H.J. Dai, J. Am. Chem. Soc. 132 (2010) 13978.
[27] P. Poizot, S. Laruelle, S. Grugeon, J.-M. Tarascon, J. Electrochem. Soc. 149 (2002) A1212.
[28] X. Fang, X. Lu, X. Guo, Y. Mao, Y.-S. Hu, J. Wang, Z. Wang, F. Wu, H. Liu, L. Chen, Electrochem. Commun. 12 (2010) 1520.
[29] K. Zhong, X. Xia, B. Zhang, H. Li, Z. Wang, L. Chen, J. Power Sources 195 (2010) 3300.

[30] K. Zhong, B. Zhang, S. Luo, W. Wen, H. Li, X. Huang, L. Chen, J. Power Sources 196 (2011) 6802.
[31] J. Guo, Q. Liu, C. Wang, M.R. Zacharia, Adv. Funct. Mater. 22 (2012) 803.
[32] C. Chae, J. Kim, J.M. Kim, Y.-K. Sun, J.K. Lee, J. Mater. Chem. 22 (2012) 17870.
[33] Y. He, L. Huang, J.S. Cai, X.M. Zheng, S.G. Sun, Electrochim. Acta 55 (2010) 1140.
[34] P.C. Lian, X.F. Zhu, H.F. Xiang, Z. Li, W.S. Yang, H.H. Wang, Electrochim. Acta 56 (2010) 834.
[35] J. Hassoun, S. Panero, P. Reale, B. Scrosati, Adv. Mater. 21 (2009) 4807.
[36] M. Imazaki, K. Ariyoshi, T. Ohzuku, J. Electrochem. Soc. 156 (2009) A780.
[37] J. Hassoun, K.-S. Lee, Y.-K. Sun, B. Scrosati, J. Am. Chem. Soc. 133 (2011) 3139.
[38] J. Hassoun, F. Croce, I. Hong, B. Scrosati, Electrochem. Commun. 13 (2011) 228.
[39] S. Brutti, J. Hassoun, B. Scrosati, C.-Y. Lin, H. Wu, H.-W. Hsieh, J. Power Sources 217 (2012) 72.
[40] W.W. Lukens, G.D. Stucky, Chem. Mater. 14 (2002) 1665.
[41] S.-R. Li, Y. Sun, S.-Y. Ge, Y. Qiao, Y.-M. Chen, I. Lieberwirth, Y. Yu, C.-H. Chen, Chem. Eng. J. 192 (2012) 226.
[42] B.R. Strohmeier, D.M. Hercules, J. Phys. Chem. 88 (1984) 4922.
[43] T.D. Schladt, T. Graf, W. Tremel, Chem. Mater. 21 (2009) 3183.
[44] B. Sun, Z.X. Chen, H.S. Kim, H. Ahn, G.X. Wang, J. Power Sources 196 (2011) 3346.
[45] K.F. Zhong, B. Zhang, S.H. Luo, W. Wen, H. Li, X.J. Huang, L.Q. Chen, J. Power Sources 196 (2011) 6802.
[46] Y. Li, B. Tan, Y. Wu, Nano Lett. 8 (2008) 265.
[47] J. Jamnik, J. Maier, Phys. Chem. Chem. Phys. 5 (2003) 5215.
[48] G. Derrien, J. Hassoun, S. Panero, B. Scrosati, Adv. Mater. 19 (2007) 2336.
[49] J. Li, H.M. Dahn, L.J. Krause, D.B. Le, J.R. Dahn, J. Electrochem. Soc. 155 (2008) A812.